Dynamical Josephson effects in $NbSe_2$

S. Tran, J. Sell, and J. R. Williams
Department of Physics, Joint Quantum Institute and the Center for Nanophysics and Advanced Materials, University of Maryland, College Park, Maryland 20742, USA

(Received 7 April 2020; accepted 25 September 2020; published 9 November 2020)

The study of superconducting materials that also possess nontrivial correlations or interactions remains an active frontier of condensed matter physics. $NbSe_2$ belongs to this class of superconductors and recent research has focused on the two-dimensional properties of this layered, superconducting material. Often, electronic transport measurements are used to investigate the superconducting properties of these materials, hence it is key to obtain a thorough understanding of transport in these systems. We investigate the transition between the superconducting and resistive state using radio-frequency AC excitation. Despite being a single piece of superconductor, the devices show novel dynamical Josephson effects behavior reminiscent of the AC Josephson effect observed in Josephson junctions. Detailed analysis uncovers the origin of this effect, identifying two types of vortex motion that categorize the transition to the normal state. Our results shed light on the nature of superconductivity in this material, unearthing exotic phenomena by exploiting nonequilibrium superconducting effects in atomically thin materials.

DOI: 10.1103/PhysRevResearch.2.043204

I. INTRODUCTION

The Bardeen–Cooper–Schrieffer (BCS) description of a superconductor provides a mean-field description of Copper pairs in a material in equilibrium. Away from equilibrium, novel superconducting phenomena can occur; the fragility of superconductivity in materials of reduced dimensions can be more susceptible to nonequilibrium effects [1,2]. The advent of atomically thin materials has ushered new platforms for studying condensed-matter physics in two dimensions. Recently, there has been a strong thrust towards isolating graphene-like materials with interactions between the carriers, allowing for the possibility of complex, correlated states at low temperatures. One such material, $NbSe_2$ [3], has a well-studied past due to the interesting states arising from the competition with a coexisting charge-density wave [4,5] and possible multiband superconductivity [6–9]. More recently, $NbSe_2$ has been studied in its two-dimensional form, where novel types of superconductivity (Ising) [10] were observed. In addition, the presence of spin-orbit interaction, enhanced in two-dimensional due to a broken in-plane mirror symmetry, provides routes to topological phases of matter in this material [11,12].

In this work we fabricate mesoscale devices formed from $NbSe_2$ thin films, focusing on the transition from the superconducting state to normal state as a function of applied DC current (I_{DC}), magnetic field B perpendicular to the surface of the $NbSe_2$ and radio frequency (RF) power P. The current-driven resistive state is found to be induced dynamic vortices, created at superconducting weak spots under the application of current to the sample. The combination of the vortex motion and RF radiation produce dynamical Josephson effects. For the first time these effects are detailed experimentally. Each result expands the knowledge of the superconducting state of $NbSe_2$, sheds light on the nature of Josephson junctions in which the superconductivity both competes with other collective phenomena, and offers a new characterization method by which information can be extracted from superconducting thin films.

In this paper, the superconducting transport properties of three devices Samples I to III [Figs. 1(b) and 1(d), see the Supplemental Material [13] to complete device details] of varying thickness are investigated. We find that magnetic fields or applied currents can drive the system out of equilibrium and these effects can alter the behavior of the current-voltage characteristics. Shown in Fig. 1(a) is a schematic of the experimental setup for measuring the superconductor-to-normal transition as a function of applied DC and AC currents. A lock-in amplifier is used to apply a DC current and 17 Hz AC current through the sample and to measure the voltage difference between leads $V1$ and $V2$. RF currents are applied to the sample via a signal generator. This signal is coupled into the sample on the same leads as the low-frequency currents via a bias-tee. The differential resistance $r = dV/dI$ versus the DC current I_{DC} can then be measured as a function of the RF frequency (f) and power (P).

When driven out of equilibrium, the dynamic incorporation of vortices into a superconductor via the applied current is known to modify the transport in superconductors. In two-dimensional superconductors where the width of the film is

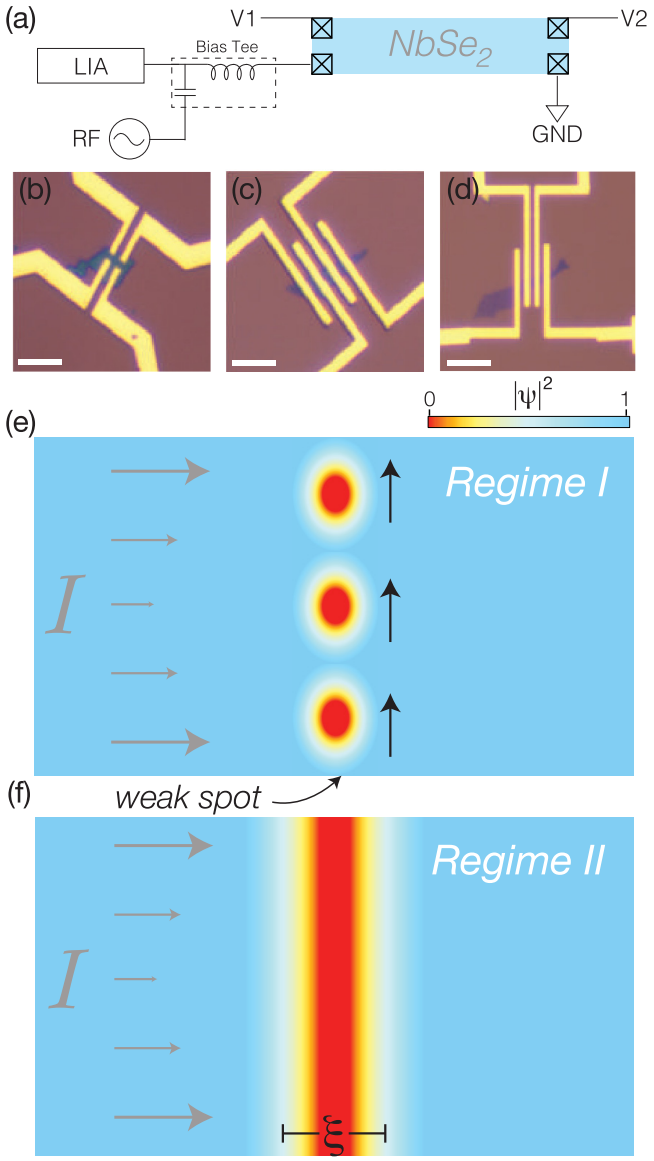

FIG. 1. (a) Schematic of measurement setup that allows for the measurement of r with a lock-in amplifier (LIA) as a function of I_{DC} and RF frequency and power. Optical images of (b) Sample I, (c) Sample II, and (d) Sample III. The scale bar in each image is 10 μm in length. (e) Schematic of the vortex production at the sample edge. Vortices nucleate at points of weak superconductivity (amplitude given in terms of superconducting order parameter amplitude $|\psi|^2$) and propagate perpendicular to the applied current. (f) As the production rate of vortices increases, vortices begin to travel in the wake of the preceding, creating a line of suppressed superconductivity. The color scale in (e), (f) goes from 0 (red, full suppression of superconductivity) to 1 (blue, no suppression).

larger than both the coherence length ξ and the penetration depth, vortices can play an important role in the transition from a superconductor to a metal [1]. As elucidated in Ref. [14], vortices can be created near the edge of the sample where the superconducting order parameter is weakest, driving the sample normal. This occurs in two stages [14]. First, vortices begin to nucleate at a spot where superconductivity is suppressed and experience a force that is perpendicular to the applied current [Fig. 1(e), called Regime I in the rest of the paper]. The vortex travels across the sample and disappears at the other edge or annihilates with an antivortex. As current increases, vortex production rate also increases and vortices begin to travel in the wake of the vortex that came before it. This produces a chain of fast (kinematic) vortices, resulting in a region of suppressed superconductivity that spans the sample width [Fig. 1(f), Regime II]. This is called a phase slip line (PSL) and it forms a Josephson junction with a length of $\sim\xi$. The effects of PSLs on DC electrical transport were recently observed in $NbSe_2$ [15]. Here we investigate each type of vortex motion and find that distinct Josephson effects characterize each regime.

II. REGIME II: PHASE SLIP LINES

It can be difficult to distinguish a PSL using electrical transport measurements, as the increase in resistance typically used to identify a PSL can occur for a variety of reasons. Here we conclusively identify a PSL by treating it as a Josephson junction. Should there be a junction created by the PSL, RF radiation mixed with the internal Josephson frequency should produce voltage steps in the I–V curve (or peaks in r)—called Shapiro steps—of height related to the applied frequency: $V = hf/2e$ [16]. This is known as the AC Josephson effect. Upon varying P, the width of each step along the I_{DC} axis follows a Bessel function dependence on P [16]. Shown in Fig. 2(a) is a numerical simulation of an overdamped Josephson junction, producing a plot of r as a function of I_{DC} and P. Plots of this type are referred to as Shapiro diagrams. Black areas are regions of $r = 0$, identifying the Shapiro steps. Peaks of nonzero values (colored purple and yellow) of r separate these black regions. Integration of this peak in r gives the value of the Shapiro step height. In this numerical simulation, integrating the peak heights $\int r dI_{DC}$ between adjacent regions of $r = 0$ along the I_{DC} axis produces the Shapiro step $hf/2e$. The step index is also shown on the diagram. It is clear that the nth step follows an nth-order Bessel function dependence on P, as expected for conventional Josephson junctions.

Figure 2(b) shows r for a $NbSe_2$ device (referred to as Sample I) as a function of the I_{DC} and P, at a fixed frequency of $f = 3$ GHz. A regular pattern of peaks in r are observed. The area under the peaks in r (corresponding to the step height in a I–V curve) have a frequency dependence. As shown in Fig. 2(c), the step height of the I–V curve obtained from integration of r produce steps heights of approximately $2\,\mu$V/GHz, identifying the peaks as Shapiro steps arising from the junction formed by the PSL.

However, there remain a marked difference between the Shapiro diagram simulation of the overdamped Josephson junction and the one for the PSL in $NbSe_2$. Two key features help to explain the deviations from a Shapiro step diagram common to conventional Josephson junctions. The first is that the Josephson junction arises only at a finite current associated with the formation of a PSL. The data of Fig. 2(b) allows for the identification of two PSLs corresponding to the transition from black to purple (at $|I_{DC}| = 140$ μA at $P = 0$ dBm) and from purple to yellow (at $|I_{DC}| = 171$ μA at the same power). It is only after these slips form that oscillations in r are observed. A broad white feature around $|I_{DC}| = 228$ μA marks

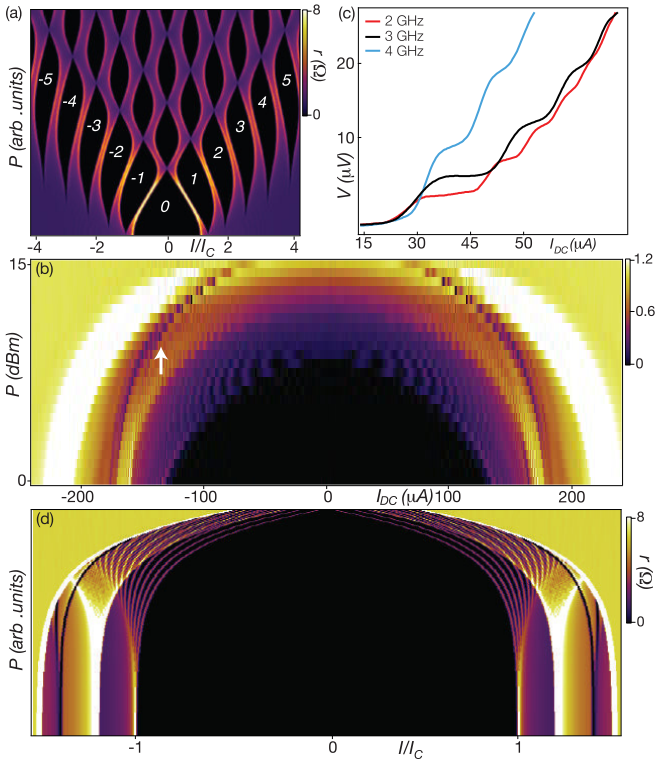

FIG. 2. (a) Shapiro diagram for a conventional overdamped Josephson junction. Step indices are shown in white. (b) Shapiro step diagram $r(I_{DC}, P)$ taken at $T = 1.2$ K. At the appearance of the first PSL, oscillations in r are observed. In addition, a depression of r (indicated with a white arrow where it crosses the transition to the normal state) possess a P dependence different than the PSL. (c) The frequency dependence of the step height increases with frequency with a magnitude of $\sim hf/2e$. (d) Simulation of coupled Eqs. (1) and (2) produces a Shapiro diagram of the simulated differential resistance r_{sim} that capture the features of the experimental diagram in (d).

the cessation of superconducting effects. One other feature, a dark depression of r (this feature is indicated by a white arrow on the positive current side), is distinct in the data of Fig. 2(b) for two reasons. It is a dip in r, rather than the increase in r due to the addition of a PSL to the device. Second, it follows a different power dependence than the PSLs and the transition to the normal state. This feature is not captured in the simulation of the Shapiro step diagrams arising solely from PSLs [13].

Discussion of the results from Regime II

In the normal state, $NbSe_2$ undergoes a charge density wave transition at a temperature of 33 K in the bulk and a temperature that is layer-number-dependent in encapsulated thin films [17]. Motion of a sliding charge density wave (CDW) is described by an equation that is very similar to Josephson junctions—each being described by a differential equation isomorphic to that of a driven pendulum. For example, Shapiro steps arise from the sliding motion of the CDW produces dip (rather than peaks, as is the case for Josephson junctions) in r under the RF excitation [18]. Any coupling between the supercurrent and the sliding motion of the CDW will modify the Shapiro diagram, similar to the modification of the motion of pendulums when they are coupled to each other. Coupling between normal electronic currents and CDW have been known for some time and produce variation of the device resistance [19]. Coupling between a supercurrent and CDW motion was theoretically considered in Ref. [20]. For a Josephson junction weak-link comprised of a CDW material, coupling between the Josephson current and the sliding motion of the CDW can affect the I–V curves. This occurs when the length of the junction (the distance between the two superconducting leads) is of order a coherence length [20]. For $NbSe_2$, this coherence length is $\sim$10 nm [21], a lengthscale difficult to achieve by conventional lithographic techniques. However, here the junction length is automatically set to this lengthscale, making the results of Ref. [20] applicable to our junctions.

The governing equations of a CDW-weak-link Josephson junction are [20]

$$I = I_C \sin\varphi + \frac{eN}{\pi}\dot{\chi} + \frac{\hbar}{2eR_N}\dot{\varphi} + I_{AC}\sin\Omega t, \tag{1}$$

$$\frac{\hbar\dot{\varphi}}{2e} = V_T \sin\chi + \frac{e}{\pi}NR_c\dot{\chi}, \tag{2}$$

where I_C and φ are the critical current and phase difference across the junction, I_{AC} and Ω are the AC drive amplitude and frequency, V_T is the threshold voltage for CDW motion, R_C is the dissipation of the CDW in motion, N is the number of 1D CDW chains, and χ is the phase of the CDW (see Ref. [13] for more detail). For our convenience we work with a dimensionless form of Eqs. (1) and (2) by setting $I_C = R_N = \hbar = e = 1$. To be explicit, we have that $I = I'/I_C$, $V_T = V_T'/I_C R_N$, $R_C = R_C'/R_N$, $\Omega = \Omega'/(2eI_C R_N/\hbar)$, where the primed terms are the physical quantities.

A simulation of Eqs. (1) and (2) which closely resembles our data is shown in [Fig. 2(d)]. Further details about the simulation are given in the Supplemental Material [13]. The simulation captures the essential features of the experimental data: a regular series of oscillations, which oscillate more rapidly when the second phase slip line appears and a strong dip corresponding to the CDW. Importantly, the dip in r only appears in the simulation when coupling to the CDW is included [13]. The results are obtained with the dimensionless parameters $R_C = 8.5$, $V_T = 1.1$, and $\Omega = 0.1$. These can be converted to physical quantities by using the critical current and normal resistance of Sample I, which we define to be the current value at which the first PSL is generated, and the measured resistance of that PSL (when there is no RF power supplied to the sample). Using the values of 167 μA and 0.35 Ohms for I_C and R_N, gives $R_C = 2.98$ Ohms, $V_T = 64.3\,\mu$V, and $\Omega' = 17.8 \times 10^9$ rad/sec (2.8 GHz). The extract frequency (2.8 GHz) is close to the experimental value of 3 GHz. The threshold voltage can also be compared to previous experiments measuring the nonlinear electrical transport that arises from the sliding motion of the CDW. Threshold electric fields have not been measured in $NbSe_2$ at this temperature due to the transition to the superconducting state. Instead the extract value is compared to a similar material, $NbSe_3$. In nanowire of $NbSe_3$, reported values of the threshold electric field are $\sim$50 V/cm. Using the coherence length

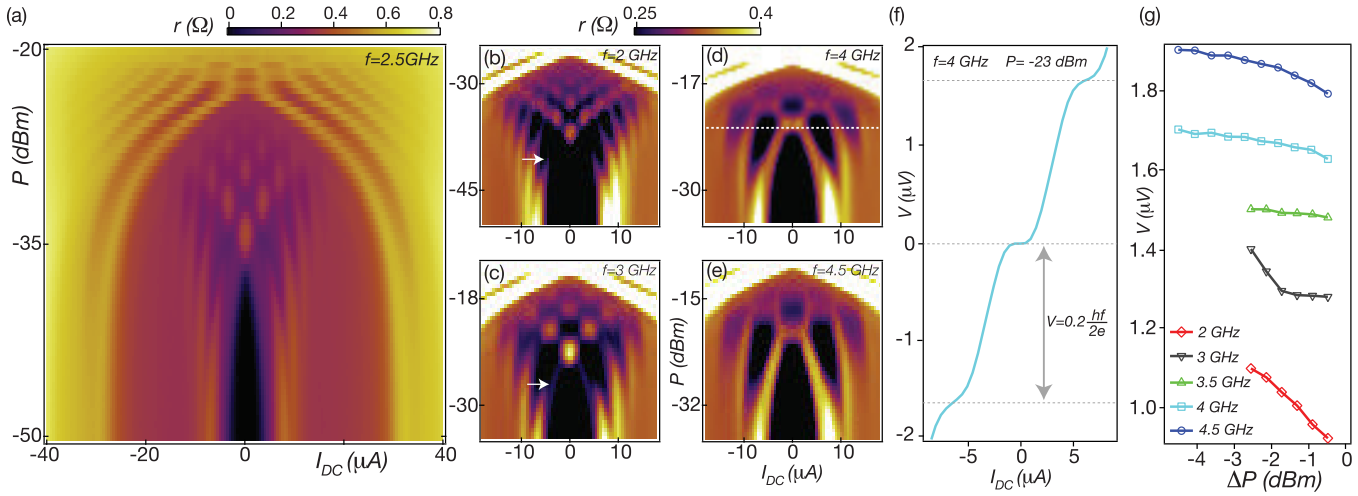

FIG. 3. (a) Shapiro step diagram for Sample II showing "inner" and "outer" Josephson features. (b)–(e) Frequency dependence of the inner features in Sample II showing a Bessel-function-like dependence of the step features. Some unconventional features are observed: a reduced step height that is not independent of power (white arrow). All graphs in (b)–(e) have axes $P(dBm)$ vs. $I_{DC}(\mu A)$. (f) Integrated I–V curve taken at $(f, P) = (4\ \text{GHz}, -23\ \text{dBm})$ showing reduced voltage steps heights. (g) Power and frequency dependence of the $0 \rightarrow -1$ step height showing a reduced step height that increases with frequency and decreases with power. The reference power is taken to be the closure of the first step. This reference power is shown for $f = 4$ GHz in (d) by the dashed white line.

(∼10 nm) of a vortex in $NbSe_2$ as the thickness of the CDW region and $V_T = 64.3\ \mu$V produces a threshold electric field of 63.4V/cm. This value is consistent with sub-10 K measurements for $NbSe_3$ nanowires [22].

III. REGIME I: INDIVIDUAL VORTEX MOTION

Individual vortex motion [Regime I, Fig. 1(e)] occurs at lower values of I_{DC} than kinematic vortices for the PSL. Voltages produced by individual vortex motion are typically two orders of magnitude smaller than the voltages produces across PSL [14], making vortices in Regime I difficult to see in electrical transport. In this section we demonstrate how RF radiation can be used to investigate vortices in Regime 1. First, to enhance the voltage produced in Regime 1, we move to thinner samples that have larger normal state resistivity [14]. In these two thinner samples (Samples II and III), more structure is measured in the Shapiro diagrams as a result of individual vortex motion. Observed in Fig. 3(a) for Sample II are two distinct collections of oscillations of r. The first we identify is due to the formation of a PSL, similar to Sample I. This transition is visible in Fig. 3(a) at a value of $|I_{DC}| = 30\ \mu A$ at $P = -45$ dBm, following a power dependence similar to what was observed for the PSL in Fig. 2(b). In addition, there are features at smaller values of $|I_{DC}|$. These features have a quantitative different Josephson behavior than the ones at larger values of $|I_{DC}|$. Henceforth, we refer to the unconventional Josephson features as "inner" features (as they occur at smaller values of $|I_{DC}|$) and those with a conventional Josephson effects as "outer" features.

The frequency dependence of the inner features are shown in Figs. 3(b) to 3(e). As the frequency increases, the peaks in r become more pronounced and the I_{DC} spacing between peaks increases. The pattern is reminiscent of the conventional Josephson junctions: the peak height of r increases with frequency and the width of the plateaus in r (called the step width) has a Bessel-function-like dependence on P [16]. The pattern observed is, however, only qualitatively similar to conventional junctions.

There are prevalent distinctions in this Shapiro diagram that are distinct from conventional Josephson junctions. First, the integrated peak height of r is substantially smaller than is expected for Shapiro steps in Josephson junctions. Shown in Fig. 3(f) is the integration of r taken at $(f, P) = (4\ \text{GHz}, -23\ \text{dBm})$. Steps in this I–V curve are visible yet occur at a reduced value of $V = 0.2\,hf/2e$. In addition the peak height is power dependent. Unlike conventional junctions where the peak height is uniform, here we observe regions where the peak height is reduced as power is increased and the step transition occurs at lower values of I_{DC}. Regions where this occurs are most prominently seen in the 2 and 3 GHz data [Figs. 3(b) and 3(c)], indicated by the white arrow. Figure 3(g) shows the power dependence of the peak height of the $0 \rightarrow -1$ step transition (i.e., the height along the peak indicated by the white arrows in Figs. 3(b) and 3(c). To accommodate the variation of power as a function of frequency, the power dependence $\Delta P = P - P_{\text{ref}}$ is measured from power of the closure of the first step [indicated by the white line in Fig. 3(d)]. The peak heights do, however, increase with increasing frequency as expected for the AC Josephson effect.

Another distinction between the inner and outer features is their respective dependence on an applied magnetic field. Contrary to the conventional Josephson effect, the inner features demonstrate an insensitivity to an applied magnetic field. By contrast, the outer features exhibit a conventional magnetic diffraction pattern expected for long Josephson junctions [16]. This contrasting behavior in a magnetic field is displayed in Figs. 4(a) and 4(b) for Samples II and III. The plots are taken under RF radiation of 5 GHz [Fig. 4(a)] and 7 GHz [Fig. 4(b)]. The outer features associated with the PSL show a diffraction pattern expected for Josephson junctions [Figs. 4(a) and 4(b)]. The inner features, however, display an entirely

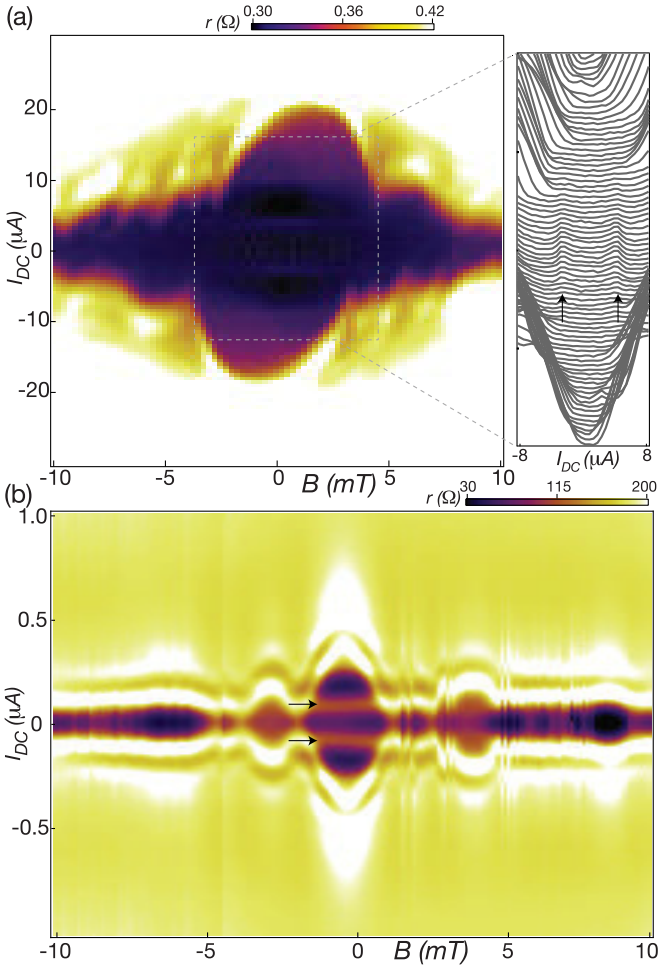

FIG. 4. (a), (b) Magnetic field dependence of the Shapiro steps for Samples II ($f = 5$ GHz, $P = -17.5$ dBm) and III ($f = 7$ GHz, $P = -10$ dBm). In addition to the Fraunhofer-like pattern observed in the outer features, magnetic-field-independent peaks in r are observed for the inner features in each sample for values of applied flux less than Φ_o (indicated in each figure by black arrows). The peaks in (a) are faint, so cuts at constant B the figure are shown on the right.

different behavior. Clear field-independent peaks in r (indicated by black arrows) that correspond to the RF generated peaks are observed over the range of magnetic field of one quantum of flux, measured by the first node in the magnetic diffraction pattern of the outer features. Beyond this field, it is difficult to differentiate the inner and outer features.

Another departure from the conventional Josephson effect is the frequency dependence of the Shapiro step diagram. The frequency dependence of the Shapiro steps are summarized in Fig. 5 for f ranging from 1 to 7 GHz for Sample III (see Ref. [13] the entire collection of data sets in this frequency window and to see the frequency-dependent Shapiro step diagrams for a conventional Josephson junction). What is observed is that the "envelope" outlining these features display a nonmonotonic dependence on P, most prominently observed for $f = 1$ [Fig. 5(a)], 3 [Fig. 5(b)], and 3.5 GHz [Fig. 5(c)]. The features first expand, then shrink towards smaller values of I_{DC} and then spread outwards again. This is contrasted by the more conventional envelope shape as a function of P seen in Figs. 5(e) and 5(f), where the envelope size continues to increase as P is increased.

Discussion of the results from Regime I

The anomalous properties seen in Regime I deserve a closer look. Two possible candidates are first identified for the origin of this effect: multiple phase slips (Josephson junctions) induced by disorder in $NbSe_2$ and Shapiro steps originating from the CDW. We can rule out these possibilities. An additional PSL is indeed possible, however, cannot explain the observed behavior. A phase-slip Josephson junction has dependence on magnetic field and does not have the frequency dependence observed in Fig. 5 [23]. Josephson behavior was observed in CDW systems: the similarity between the equations governing the CDW and Josephson junction dynamics allows for Shapiro steps to be observed in materials like $NbSe_3$ [24]. The primary difference is that the dynamical equation for CDW is one for the voltage produced by the sliding mode of the CDW and the differential resistance is locally a maximum in the regions of the Shapiro steps, separated by regions of lower resistance [13]. Further, there is no anomalous frequency dependence as we observed. We also note that the AC-dependent voltage step height is of order 10 mV/GHz [24], roughly three orders of magnitude higher than expected for Josephson junctions and four orders of magnitude greater than the typical peak height is observed in Samples II and III.

The magnetic-field independence and anomalous frequency dependence suggests that dynamical mode locking distinct from that in a Josephson junction is responsible for the observation. Another mechanism for the production of Shapiro steps is possible in superconductors: the collective motion of a vortex lattice in a periodic potential also gives rise to Shapiro steps [25,26]. Hence we turn towards the production of vortices at the edge of the sample [Fig. 1(f)] as a source of the steps. The dynamics of current-induced vortices would not be affected by the small values of B explored in Fig. 4, therefore would explain the field independence observed in experiment.

The AC Josephson effect is a subset of a larger group of systems where motion occurs in periodic potentials. When driven sinusoidally these systems can produce Shapiro steps, albeit with a different relationship between the frequency and voltage (or between the equivalent variables for the system) compared to Josephson junctions. For example, Shapiro steps in coupled superconducting thin films can have a frequency-to-voltage relation that depends on the relative velocity of vortices in each film Ref. [27].

To understand how Shapiro steps may arise from production of vortices at the edge of the sample, it is important to look at how vortices enter the sample in a mutliband superconductor like $NbSe_2$. The dynamics of sample-edge vortex production is markedly different in multiband superconducting materials. For a superconductor with two-bands, a vortex is a composite of two vortices, one from each band [9]. The winding numbers on each band can be different, allowing for fractional flux to be associated with each vortex [9,28]. However, an attractive force between vortices from different bands pins the two vortices together in a composite vortex

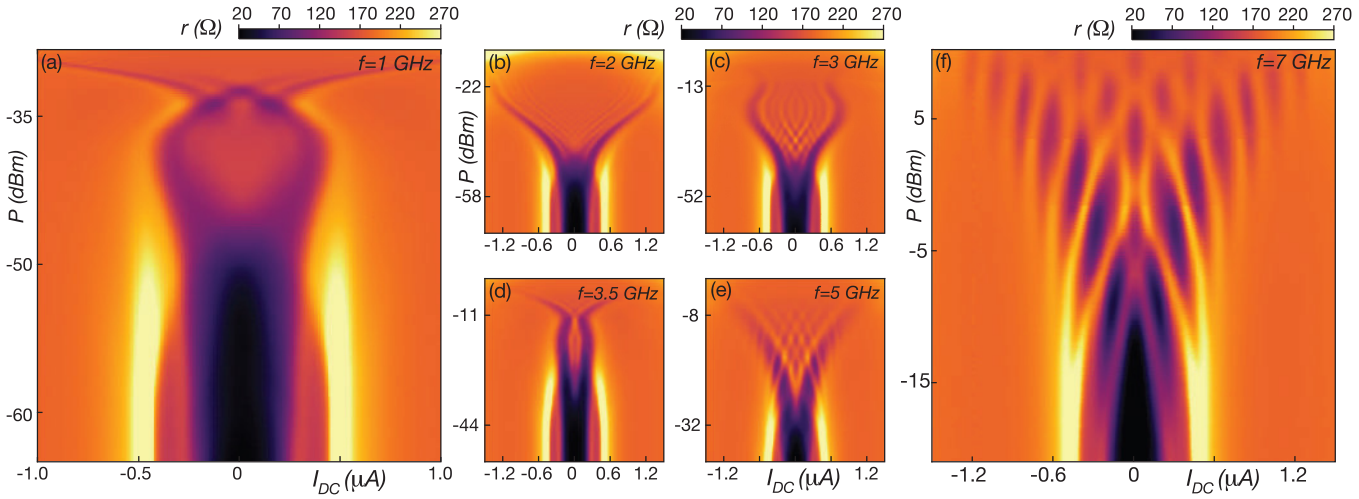

FIG. 5. (a)–(f) Shapiro step diagrams for Sample III demonstrating the frequency dependence of Josephson features for f from 1 to 7 GHz. All plots have axes P vs. I_{DC}, with panel (a) being plotted on a smaller frequency range than panels (b) to (e). The Shapiro steps are shown to shrink and then expand with increasing f, contrary to the conventional Josephson effect where Shapiro steps only get spread out with increasing f. The Shapiro step diagrams also exhibit different structures when comparing panels (a)_ to (c) ($f < 3.5$ GHz) to panels (e), (f) ($f > 3.5$ GHz).

with a single quantum of flux when the superconductor is in equilibrium [29]. When the superconductor is driven from equilibrium, dissociation of the composite vortex is possible.

In our samples, dissociation can happen for two reasons. First the Bean-Livingston barrier for entry into the superconductor is, in general, different for the two bands, hence can promote dissociation at the sample edge [30]. Second, once in the sample, the velocity of vortex propagation will be different for each vortex associated with the two bands [29]. Thus, even if a composite vortex enters the sample, dissociation can occur due to different propagation velocity. In the later of these, Shapiro steps have been predicted: the faster fractional vortices will pass over the periodic potential provided by the slower vortices. The step height in this scenario is set by the difference in propagation velocity, rather than the actual velocity of the vortex. This allows for the reduction of the step height in proportion to $(1\text{-}v_2/v_1)$ [29], where v_i is the velocity of the vortex in the ith band. The relative velocity of the two bands is given by $v_2/v_1 = (\xi_1/\xi_2)^2 = (\Delta_2/\Delta_1)^2$. The ratio of the superconducting order parameter of the two Nb-derived bands has been measured by angle-resolved photoemission spectroscopy (ARPES), finding a ration of 0.9 between these two bands [6]. This would produce an 80% reduction of the Shapiro step height, consistent with our observations [Fig. 3(f)]. This two-band model may also explain the power and I_{DC} dependence of the peak height. Vortices in a multiband superconductor will experience two forces: one from the supercurrent, which is proportional to I_{DC}, and the attractive interaction between vortices at different bands. At low values of I_{DC}, the ratio between force from the supercurrent and attractive vortex interactions is low. The attractive force reduces the relative velocity between the vortices of the two bands (i.e., the ratio v_2/v_1 is increased) and decreases the step height. As I_{DC}, the force from the supercurrent can dominate, resulting in a decrease of v_2/v_1 and increase in step height.

Finally, the anomalous power dependence observed in the Shapiro diagram can also be explained in this context. Motion in a periodic potential, which includes the attractive interaction between the two vortices comprising the composite vortex, is described by the Frenkel-Kontorova model. Numerical simulations of this model demonstrated oscillations of the step width and depinning current (the envelope described above) as a function of power and frequency [31]. Specifically, oscillations occur in the low-frequency regime ($f < 0.16$), where f is the frequency of the drive relative to a characteristic frequency of the system, f_C. Oscillations cease when the frequency is increased. This is consistent with the experimental observations. Sample II ($f_C = 6.7$ GHz, see Ref. [13] for calculations of f_C) is explored in the frequency regime above the oscillation region (f relative to the characteristic frequency is explored in the range 0.18 to 0.75). Sample III ($f_C = 21.2$ GHz, explored in the range 0.05 to 0.28) observes results consistent with theory: oscillations are observed in the envelope until $f = 4$ GHz (0.18 relative to the characteristic frequency) after which the oscillations exhibit a monotonic dependence on frequency.

IV. CONCLUSION

In this paper, we detailed a method which utilizes transport in the presence of RF radiation to probe the role of vortices in the transition from the superconducting to the normal state. The dynamic effects of vortex motion give rise to unconventional AC Josephson effects. While the origin of these effects needs further theoretical work, we demonstrate how CDW motion and multiband superconductivity can produce two new effects observed in this work. The first is a coupling of the supercurrent in a Josephson junction to the sliding motion of a charge density wave. This was facilitated by the small length of a phase-slip Josephson junction. The second, observed in thinner samples, was the interplay between vortex production at the edge of the sample, giving rise to Shapiro steps that were smaller than expected, insensitive to magnetic field and possessing an anomalous behavior as a function of power,

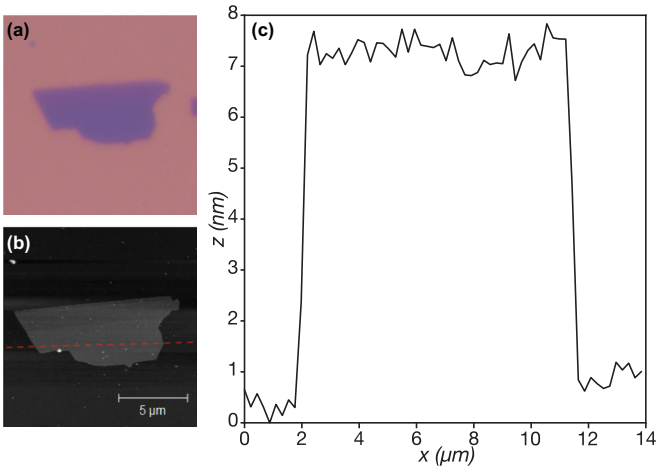

FIG. 6. (a) Optical and (b) AFM images of a thinner flake, (c) the height difference z of the flake relative to the background as a function of distance x along the dotted red line. The flake has a thickness of roughly 7 nm.

I_{DC}, and frequency. The origin of this effect was suggested to be the dissociation of composite vortices in a multiband superconductor driven from its equilibrium state. Both of these results may further the understanding of $NbSe_2$ and demonstrates the power of investigating thin-film superconducting materials out of equilibrium.

ACKNOWLEDGMENTS

We thank Sergiy Krylyuk and Albert Davydov for technical discussion including materials preparation. This work was sponsored by the National Science Foundation Physics Frontier Center at the Joint Quantum Institute (PHY-1430094). Funding for the AFM shared facility used in this research was provided by NSF under Award No. CHE-162688.

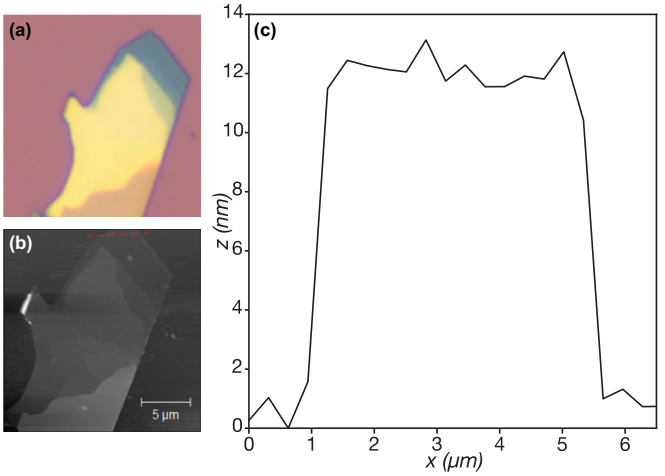

FIG. 7. (a) Optical and (b) AFM images of a thicker flake, (c) the height difference z of the flake relative to the background as a function of distance x along the dotted red line. The flake has a thickness of roughly 12 nm.

TABLE I. Characterization of Samples I to III.

Sample name	Thickness	Lead configuration	Opticalimage
Sample I	∼10 nm	Box	
Sample II	∼9 nm	Linear	
Sample III	∼6 nm	Linear	

APPENDIX A: FLAKE THICKNESSES

To minimize the exposure of our devices to the atmosphere, we did not perform atomic force microscopy (AFM) on the flakes during the fabrication process. Because of this, we do not know the exact thicknesses of our devices. Measurements of the sample thicknesses after the transport measurements are likely to include an oxide. To estimate the thicknesses of our samples we performed AFM measurements of flakes which display similar optical contrast. To minimize the exposure of these flakes to the atmosphere, we kept the time between exfoliation and AFM measurement to within one hour. Presented in Fig. 6 are [Fig. 6(a)] optical, [Fig. 6(b)] AFM images of a thinner flake, and [Fig. 6(c)] the height difference of the flake, z, measured with respect to the background. The height difference is plotted as a function of distance from left to right along the dotted red line x. The height difference suggests that our flakes of similar color are around 7-nm thick. Similarly, presented in Fig. 7 are the same quantities for one of the thicker flakes. The profile suggests that our thicker flakes are around 12 nm. Figure 6 closely resembles our Samples II and III, and Fig. 7 closely resembles Sample I.

APPENDIX B: DEVICE CHARACTERISTICS

The devices fabricated employ two different lead configurations: either the four leads enclose a 3 μm $\times$ 3 μm box

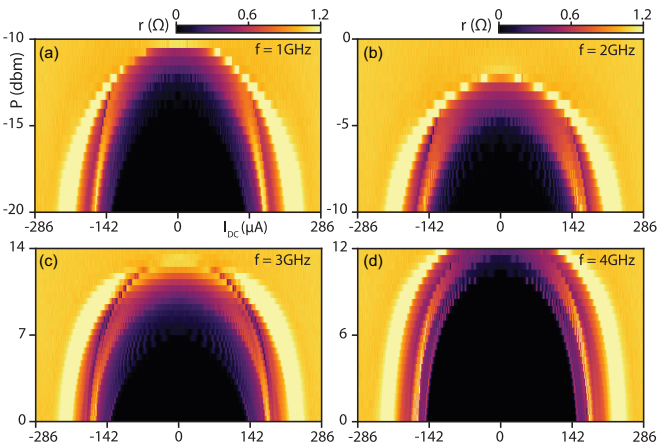

FIG. 8. Additional data for Sample I (a) to (d) plots of differential resistance $r(I_{DC}, P)$ as a function of bias current I_{DC}, and RF power P for f from 1 to 4 GHz. The scale bar is the same for all plots.

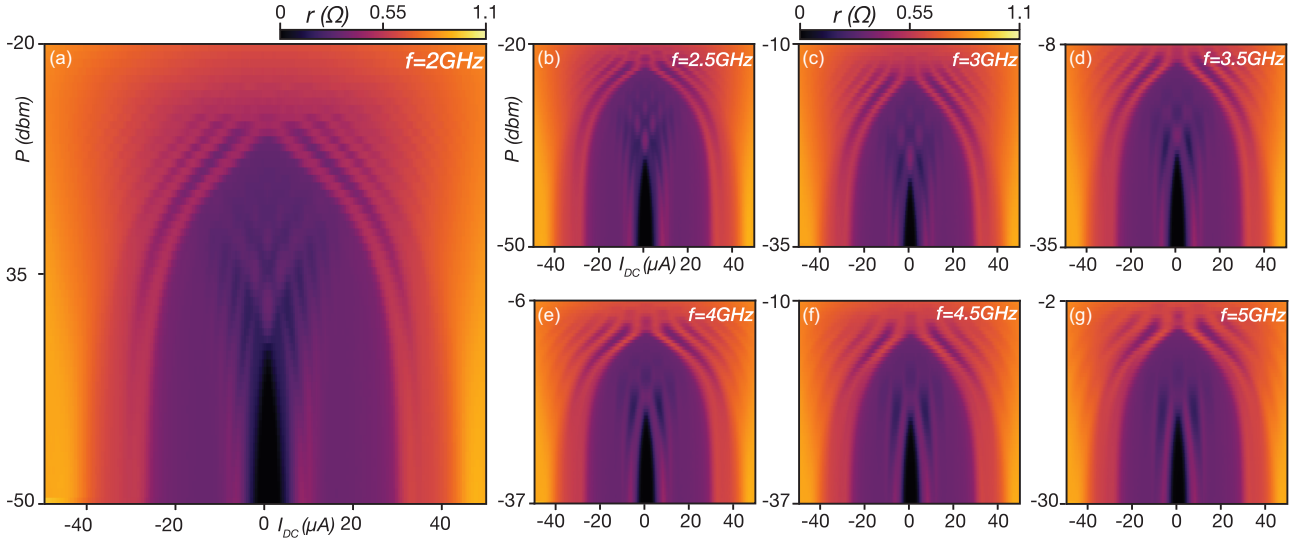

FIG. 9. Additional RF data for Sample III of the main article, (a) to (g) plots of $r(I_{\rm DC}, P)$ for f from 2 to 5 GHz. The scale bar is the same for all plots.

on the flake (referred to as the box configuration) or consecutively span the length of the flake (referred to as the linear configuration). Summarized in Table I below are our samples by their thicknesses, lead configurations, and optical images. For reference, the scale bars in the optical images are 10 microns long.

APPENDIX C: ADDITIONAL DATA

In this section are additional data for Samples I to III. Plots of differential resistance r as a function of RF power P along the y-axis (the values of P do not take into account any attenuation incurred from the path down the cryostat from the microwave generator to the sample), and bias current $I_{\rm DC}$ along the x-axis for various RF frequencies f are shown. We use standard AC lock-in techniques to measure the four-terminal differential resistance of our devices. The DC bias currents are supplied by a Yokogawa GS200 (voltage output configuration) with a bias resistor.

Shown in Figs. 8(a) to 8(d) are plots of r for Sample I for different f of 1, 2, 3, and 4 GHz. These measurements were taken at a temperature of approximately 1.2 K. From the plots we see two regions of oscillations in r (i.e., Shapiro steps) which have different scaling with P and f. In addition to these Shapiro steps, a dip in r (which appears as a dark line in the color plot) is observed in the region where a second phase slip line (PSL) is formed. This feature scales differently from the Shapiro steps with P, and has a dependence on f, as seen for $f = 2$ GHz and 3 GHz. A possible origin of the feature is discussed in the next section.

Shown in Fig. 9 are plots of r for Sample III with different applied microwave frequencies f, ranging from 2 to 5 GHz. The measurements were taken at a temperature of 1.2 K. Like Sample II, there are also two regions of Shapiro steps, which we refer to as the "inner" (those within the purple region) and "outer" (those within the orange region) features. These Shapiro steps demonstrate conventional Josephson behavior, as seen by the increase in width of the step with increasing f. In addition to these RF measurements, perpendicular magnetic field (normal to the sample surface) measurements with applied microwaves were also performed. Shown in Fig. 10 are plots of r as a function of magnetic field B along the x-axis, and $I_{\rm DC}$ along the y-axis for Sample II with Fig. 10(a) an applied $f = 2.5$ GHz at $P = -30$ dbm, and Fig. 10(b) an applied RF frequency of 5 GHz at $P = -17.5$ dbm. Both plots demonstrate an expected Fraunhofer-like diffraction pattern in the outer features. However, the inner features demonstrate an unexpected weak magnetic field dependence within the first lobe of the diffraction pattern. Line cuts of these weakly dependent peaks are presented in the main article.

Additional data for Sample III are shown in Fig. 11. The device was measured for RF frequencies ranging from $f =$ 1 to 7 GHz. An unusual feature that can be seen is that the "envelope" which encloses the inner features has an oscillatory behavior as a function of frequency. At the highest frequencies, the envelope no longer oscillates and maintains its shape. Furthermore, the Shapiro steps become nested within one another as the RF frequency is increased. In contrast to our

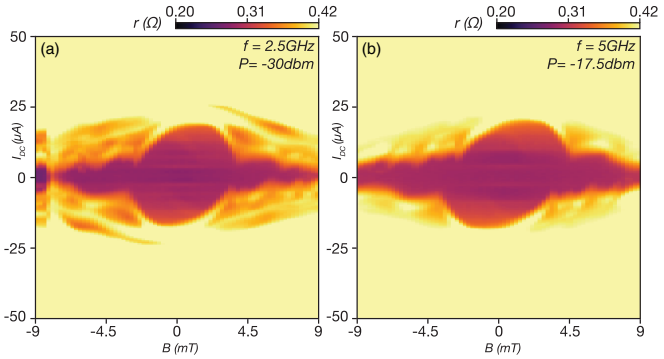

FIG. 10. Perpendicular magnetic field measurements of $r(I_{\rm DC}, P)$ for Sample II with applied microwaves of (a) $f = 2.5$ GHz at $P = -30$ dbm, and (b) $f = 5$ GHz at $P = -17.5$ dbm. The scale bar is the same for all plots.

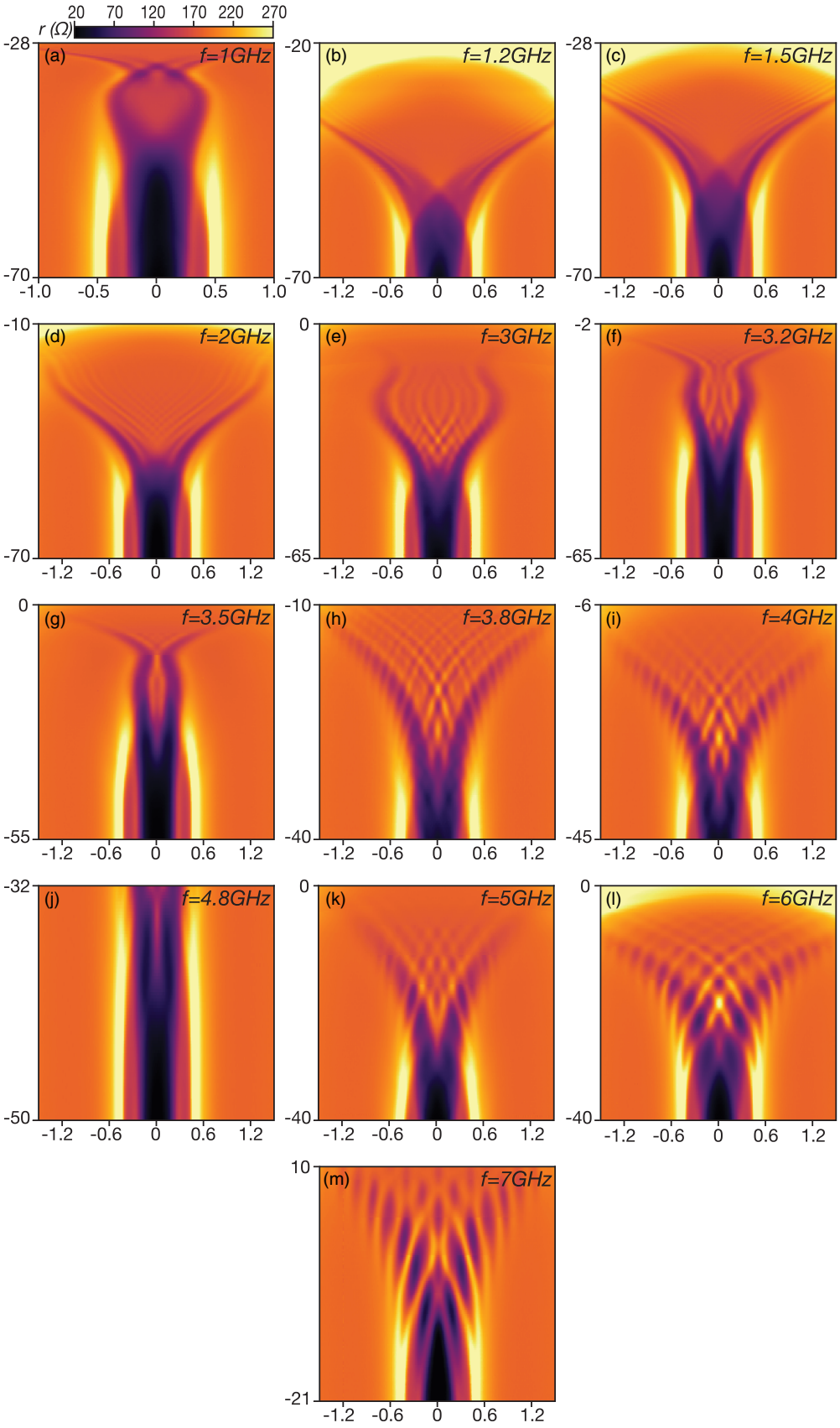

FIG. 11. Additional data for Sample III of the main article, (a) to (m) plots of $r(I_{DC}, P)$ for values of f ranging from 1 to 7 GHz. The scale bar is the same for all plots.

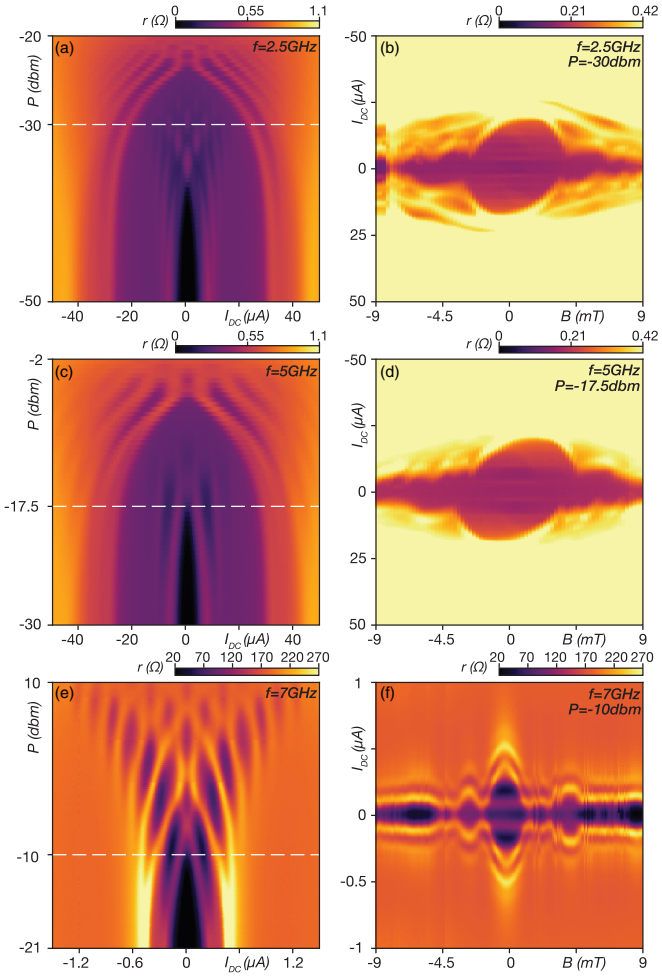

FIG. 12. Side-by-side comparison of RF data and perpendicular magnetic field data for Samples II (a) to (d) and III (e), (f) of the main article. The magnetic field data were taken along the cut indicated by the dashed white lines.

previous devices, this device was measured at roughly 56 mK as opposed to 1.2 K and did not display a zero resistance state. Finally, we summarize our magnetic field measurements with applied microwaves in Fig. 12. The dashed lines indicate where on the plots of r as a function P were the magnetic field measurements performed.

APPENDIX D: SIMULATIONS OF CHARGE DENSITY WAVES SYSTEMS/RESISTIVELY SHUNTED JUNCTION MODEL (SAMPLE I)

To understand some aspects of our data, we use a slightly modified version of the resistively shunted junction (RSJ) model which incorporates charge density waves (CDW) [20]. The equations of the system are given by

$$I_{\rm DC} = I_C \sin\varphi + \frac{eN}{\pi}\dot{\chi} + \frac{\hbar}{2eR_N}\dot{\varphi}, \tag{D1}$$

$$\frac{\hbar\dot{\varphi}}{2e} = V_T \sin\chi + \frac{e}{\pi}NR_C\dot{\chi}, \tag{D2}$$

where φ and χ are the phases of the Josephson junction and CDW, respectively, V_T is the threshold voltage required to

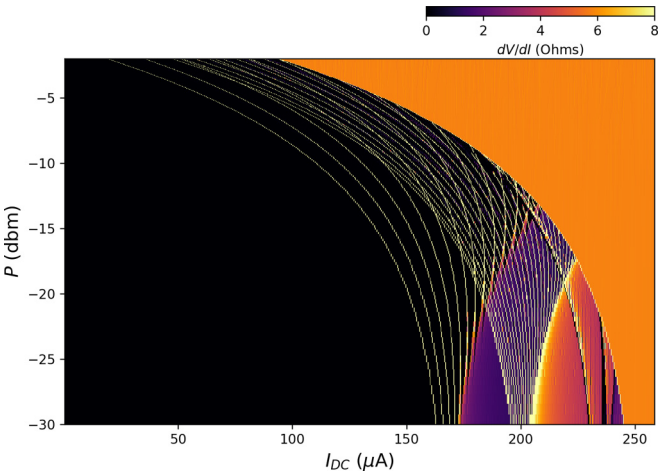

FIG. 13. Numerical simulation of $dV/dI[P, I_{\rm DC}]$ using Eqs. (4) to (6) (assuming a normal state transition for the entire flake) for $R_C = 8.5$ (2.97 Ohms), $V_T = 1.1$ (64.3 μV). Three sets of Shapiro steps are observed, two of which correspond to the AC Josephson effect while the remainder corresponds to CDW motion. The inclusion of a normal state transition masks the CDW Shapiro steps.

de-pin the CDW and start a sliding motion which carries current, N is number of chains of the CDW material and R_C is a dissipative term of the CDW. These equations do not account for any AC driving term. To account for this part of our experiment, we can modify Eq. (1) by adding an AC current term $I_{\rm AC}\sin(2\pi f_{\rm app}t)$ where $I_{\rm AC}$ is the magnitude of the AC current and $f_{\rm app}$ is the frequency from experiment

$$I_{\rm DC} = I_C \sin\varphi + \frac{eN}{\pi}\dot{\chi} + \frac{\hbar}{2eR_N}\dot{\varphi} + I_{\rm AC}\sin(2\pi f_{\rm app}t). \tag{D3}$$

To model our data, we have to make some assumptions. The first assumption is that the generation of a PSL corresponds to a Josephson junction (JJ) whose I_CR_N product is determined by the current needed to generate the PSL and the measured resistance of that PSL. Furthermore, we assume that the generation of additional PSLs creates JJs with different I_CR_N products that are coupled to the previous ones in series. Our data typically demonstrate two PSLs, so we assume that we are working with two JJs in series but there is no additional Josephson coupling between them. Finally, we assume that there is only CDW coupling in the second junction with the larger I_CR_N product. To be more explicit, we have that the first junction evolves according to

$$I_{\rm DC} = I_{C,1}\sin\varphi_1 + \frac{\hbar}{2eR_{N,1}}\dot{\varphi}_1 + I_{\rm AC}\sin(2\pi f_{\rm app}t), \tag{D4}$$

while the second junction evolves according to

$$I_{\rm DC} = I_{C,2}\sin\varphi_2 + \frac{eN}{\pi}\dot{\chi} + \frac{\hbar}{2eR_{N,2}}\dot{\varphi}_2 + I_{\rm AC}\sin(2\pi f_{\rm app}t), \tag{D5}$$

and has a CDW coupling given by

$$\frac{\hbar\dot{\varphi}_2}{2e} = V_T\sin\chi + \frac{e}{\pi}NR_C\dot{\chi}. \tag{D6}$$

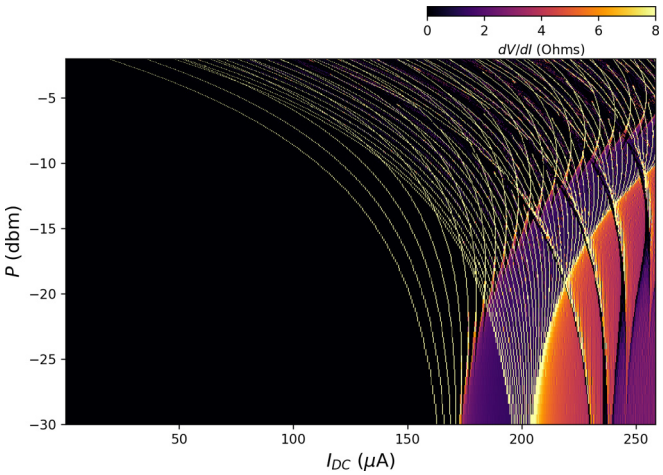

FIG. 14. Numerical simulation of $dV/dI[P, I_{\rm DC}]$ using Eqs. (4) to (6) (without assuming a normal state transition for the entire flake) for $R_C = 8.5$ (2.97 Ohms), $V_T = 1.1$ (64.3 μV). Higher-order Shapiro steps due to CDW motion are not masked by a normal state transition as in Fig. 13.

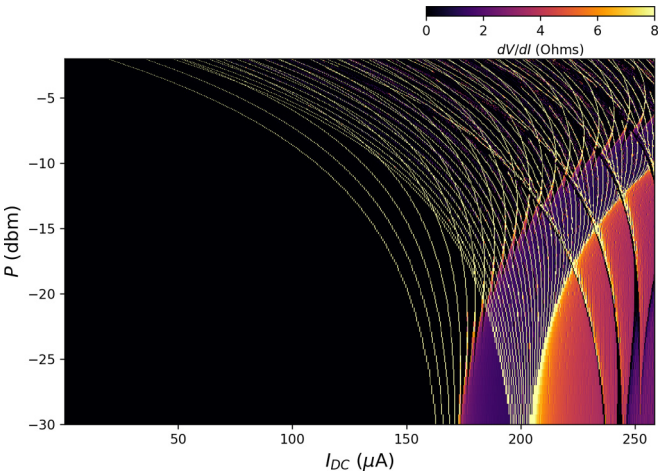

FIG. 16. Numerical simulation of $dV/dI[P, I_{\rm DC}]$ using Eqs. (4) to (6) for $R_C = 8.5$ (2.97 Ohms), $V_T = 1.2$ (70.1 μV). There is a slight shift in the Shapiro step pattern of the CDW when compared to Fig. 14.

For our convenience, we work with dimensionless quantities by setting $\hbar = e = I_{C,1} = R_{N,1} = 1$ (the values of $I_{C,2}$ and $R_{N,2}$ are scaled as some constant times $I_{C,1}$, $R_{N,1}$). This is effectively setting $I = I'/I_{C,1}$, $I_{\rm AC} = I'_{\rm AC}/I_{C,1}$, $V_T = V'_T/(I_{C,1}R_{N,1})$, $R_C = R'_C/R_N$, $f_{\rm app} = f'_{\rm app}/(2eI_{C,1}R_{N,1}/\hbar)$, and $t = (2eI_{C,1}R_{N,1}/\hbar)t'$ where the primed terms are the physical quantities. The quantity $2eI_CR_N/\hbar$ is typically known as the characteristic frequency ω_C (in rads/s) of the junction. To get physical values from these dimensionless parameters, we can simply replace I_C and R_N with the experimental value and solve for the relevant primed quantity.

To numerically solve these equations, we employ a fourth-order Runge-Kutta method to evolve the phases. The time resolution of our algorithm was $h = \pi/(650 * \omega_{C,1})$. We let the model evolve freely up to dimensionless time $t = (\omega_{C,1}t') = 1000$, where we define the phase and time at this point to be stable. After this, we let t evolve up to $t = 5000$, keeping track of the times (and values of the phase) when the phase has evolved within $2\pi n$ multiples of its stable value. The voltages V'/I_CR_N are calculated by taking an average of $(\varphi^{(n)} - \varphi_s)/(t^{(n)} - t_s)$, where $\varphi^{(n)}$ and $t^{(n)}$ the values of the phases and times when the phase is within $2\pi n$ multiples of its stable value, and φ_s and t_s are the stable phase and time. Finally, with the voltages V'/I_CR_N we can calculate the dimensionless differential resistance by doing the calculation $dV'/I_CR_N/(dI) = dV'/I_CR_N/(dI'/I_C) = (dV'/dI')/R_N$.

In Figs. S8 and S9 we show the results of our simulations of $dV'/dI'/R_N$ which best match our data for Sample I. These are plotted as a function of $I_{\rm DC}$ and P. These were performed with $R_C = 8.5$ and $V_T = 1.1$. To convert these values to real values, we note for Sample I that the critical current is estimated to be $I_C \approx 167\,\mu$A and the normal resistance to be $R_N \approx 0.35$ Ohms, as determined by differential resistance

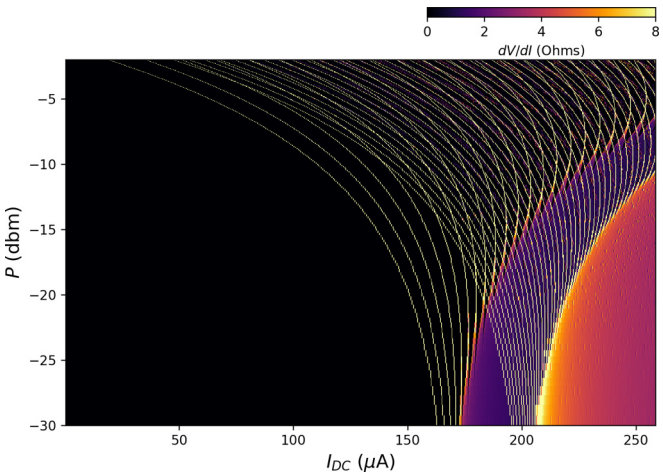

FIG. 15. Numerical simulation of $dV/dI[P, I_{\rm DC}]$ using Eqs. (4) to (6) and turning off the CDW coupling ($\chi = 0$ for all times). The simulation reproduces the Shapiro step profile of the AC Josephson effect.

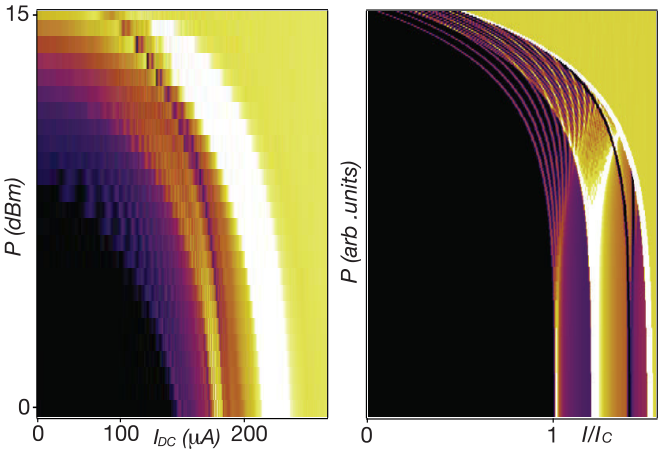

FIG. 17. Direct comparison between experiment [(a), reproduced from Fig. 2(b) in the paper] and (b) the best-matched simulation.

with no RF excitation. To convert from our simulation I_{AC} to P (dbm), we assume that the power (in Watts) delivered to the junction is due to joule heating across the resistance of the lines in our cryostat, which is roughly 25 kOhms. The conversion of Watts to dbm is given by the expression $P = 30 + 10\log_{10} P_J$, where P_J is the power due to Joule heating. The only difference between Figs. 13 and 14 is the incorporation of a third peak which is meant to mimic the normal state transition of the entire flake. As can be seen, the inclusion of a normal state transition plays a simple role of masking the features at higher DC bias. Therefore we exclude a normal station transition in our simulations for clarity. The promising feature of these simulations are the three sets of Shapiro steps, two of which display peaks in the differential resistance while the remainder demonstrates dips. The origin of the Shapiro steps which are separated by peaks is due to the usual AC Josephson effect. The reason they display a different Shapiro step profile is due to the difference in characteristic frequencies (where the second junction has a higher characteristic frequency, hence more steps).

The Shapiro steps which are separated by dips in the differential resistance are understood to arise from CDW motion. The simplest way to confirm this is to remove the CDW coupling of the second junction, and reproduce the Shapiro step profile of the AC Josephson effect. The results of this are shown in Fig. 15. Another way we can confirm the CDW nature is to tune the CDW parameters and see if the features change in a way we would expect. In particular, the threshold voltage V_T sets a DC current value at which the features first appear. We can shift the position of the features with respect to I by fixing R_C and varying V_T. The results for $R_C = 8.5$ and $V_T = 1.2$ are shown in Fig. 16. Finally, we make a direct comparison between the data from Sample I and the best-matched simulation in Fig. 17.

[1] M. Tinkham, *Introduction to Superconductivity* (Dover, New York, 1996), Chap. 11.

[2] R. Tideicks, *Current-Induced Nonequilibrium Phenomena in Quasi-One-Dimensional Superconductors*, Springer Tracts in Modern Physics, (Springer, New York, 1990).

[3] A. V. Koloboc and J. Tominaga, *Two-Dimensional Transition-Metal Dichalcogenides* (Spinger, New York, 2016).

[4] M. M. Ugeda, A. J. Bradley, Y. Zhang, S. Onishi, Y. Chen, W. Ruan, C. Ojeda-Aristizabal, H. Ryu, M. T. Edmonds, H.-Z. Tsai, A. Riss, S.-K. Mo, D. Lee, A. Zettl, Z. Hussain, Z.-X. Shen, and M. F. Crommie, Characterization of collective ground states in single-layer $NbSe_2$, Nat. Phys. **12**, 92 (2016).

[5] C.-S. Lian, C. Si, and W. Duan, Unveiling charge-density wave, superconductivity, and their competitive nature in two-dimensional $NbSe_2$, Nano Lett. **18**, 2924 (2018).

[6] T. Yokoya, T. Kiss, A. Chainani, S. Shin, M. Nohara, and H. Takagi, Fermi surface sheet-dependent superconductivity in $2H$-$NbSe_2$, Science **294**, 2518 (2001).

[7] E. Boaknin, M. A. Tanatar, J. Paglione, D. Hawthorn, F. Ronning, R. W. Hill, M. Sutherland, L. Taillefer, J.f Sonier, S. M. Hayden, and J. W. Brill, Heat Conduction in the Vortex State of $NbSe_2$: Evidence for Multiband Superconductivity, Phys. Rev. Lett. **90**, 117003 (2003).

[8] T. Dvir, F. Massee, L. Attias, M. Khodas, M. Aprili, C. H. L. Quay, and H. Steinberg, Spectroscopy of bulk and few-layer superconducting $NbSe_2$ with van der Waals tunnel junctions, Nat. Commun. **9**, 598 (2018).

[9] Y. Tanaka, Soliton in Two-Band Superconductor, Phys. Rev. Lett. **88**, 017002 (2001).

[10] X. Xi, Z. Wang, W. Zhao, J.-H. Park, K. T. Law, H. Berger, L. Forró, J. Shan, and K. F. Mak, Ising pairing in superconducting $NbSe_2$ atomic layers, Nat. Phys. **12**, 139 (2016).

[11] W.-Y. He, B. T. Zhou, J. J. He, N. F. Q. Yuan, T. Zhang, and K. T. Law, Magnetic field driven nodal topological superconductivity in monolayer transition metal dichalcogenides, Commun. Phys. **1**, 40 (2018).

[12] D. Shaffer, J. Kang, F. J. Burnell, and R. M. Fernandes, Crystalline nodal topological superconductivity and Bogolyubov Fermi surfaces in monolayer $NbSe_2$, Phys. Rev. B **101**, 224503 (2020).

[13] See Supplemental Material at http://link.aps.org/supplemental/10.1103/PhysRevResearch.2.043204 for additional information on the data and simulations, available at the time of publication.

[14] G. Berdiyorov, K. Harrabi, F. Oktasendra, K. Gasmi, A. I. Mansour, J. P. Maneval, and F. M. Peeters, Dynamics of current-driven phase-slip centers in superconducting strips, Phys. Rev. B **90**, 054506 (2014).

[15] N. Paradiso, A.-T. Nguyen, K. E. Kloss, and C. Strunk, Phase slip lines in superconducting few-layer $NbSe_2$ crystals, 2D Mater. **6**, 025039 (2019).

[16] A. Barone and G. Paternò, *Physics and Applications of the Josephson Effect* (Wiley-Interscience, Toronto, 1982).

[17] X. Xi, L. Zhao, Z. Wang, H. Berger, L. Forró, J. Shan, and K. F. Mak, Strongly enhanced charge-density-wave order in monolayer $NbSe_2$, Nat. Nano. **10**, 765 (2015).

[18] S. E. Brown, G. Mozurkewich, and G. Grüner, Subharmonic Shapiro Steps and Devil's Staircase Behavior in Driven Charge-Density-Wave Systems, Phys. Rev. Lett. **52**, 2277 (1984).

[19] G. Grüner, The dynamics of charge-density waves, Rev. Mod. Phys. **60**, 1129 (1988).

[20] M. I. Visscher and B. Rejaei, Josephson Current through Charge Density Waves, Phys. Rev. Lett. **79**, 4461 (1997).

[21] M. S. El-Bana, D. Wolverson, S. Russo, G. Balakrishnan, D. Mck Paul, and S. J Bending, Superconductivity in two-dimensional $NbSe_2$ field effect transistors, Supercond. Sci. Techno. **26**, 125020 (2013).

[22] Y. S. Hor, Z. L. Xiao, U. Welp, Y. Ito, J. F. Mitchell, R. E. Cook, W. K. Kwok, and G. W. Crabtree, Nanowires and nanoribbons of charge-density-wave conductor $NbSe_3$, Nano Lett. **5**, 397 (2005).

[23] A. G. Sivakov, A. M. Glukhov, A. N. Omelyanchouk, Y. Koval, P. Müller, and A. V. Ustinov, Josephson Behavior of Phase-Slip Lines in Wide Superconducting Strips, Phys. Rev. Lett. **91**, 267001 (2003).

[24] A. Zettl and G. Grüner, Phase coherence in the current-carrying charge-density-wave state: Ac-dc coupling experiments in $NbSe_3$, Phys. Rev. B **29**, 755 (1984).

[25] A. T. Fiory, Quantum Interference Effects of a Moving Vortex Lattice in Al Films, Phys. Rev. Lett. **27**, 501 (1971).

[26] L. Van Look, E. Rosseel, M. J. Van Bael, K. Temst, V. V. Moshchalkov, and Y. Bruynseraede, Shapiro steps in a superconducting film with an antidot lattice, Phys. Rev. B **60**, R6998(R) (1999).

[27] A. Gilabert, I. K. Shuller, V. V. Moshchalkov, and Y. Bruynseraede, New Josephson-like effect in a superconducting transformer, Appl. Phys. Lett. **64**, 2885 (1994).

[28] E. Babaev, Vortices with Fractional Flux in Two-Gap Superconductors and in Extended Faddeev Model, Phys. Rev. Lett. **89**, 067001 (2002).

[29] S.-Z. Lin and L. N. Bulaevskii, Dissociation Transition of a Composite Lattice of Magnetic Vortices in the Flux-Flow Regime of Two-Band Superconductors, Phys. Rev. Lett. **110**, 087003 (2013).

[30] M. A. Silaev, Stable fractional flux vortices and unconventional magnetic state in two-component superconductors, Phys. Rev. B **83**, 144519 (2011).

[31] B. Hu and J. Tekic, Amplitude and frequency dependence of the Shapiro steps in the dc- and ac-driven overdamped Frenkel-Kontorova model, Phys. Rev. E **75**, 056608 (2007).